

Search for the Higgs boson in the all-hadronic final state using the full CDF data set

CDF Collaboration

T. Aaltonen²¹ B. Álvarez González⁹ S. Amerio⁴⁰ D. Amidei³² A. Anastassov¹⁵
A. Annovi¹⁷ J. Antos¹² G. Apollinari¹⁵ J.A. Appel¹⁵ A. Apresyan^{44,jj} T. Arisawa⁵⁴
A. Artikov¹³ J. Asaadi⁴⁹ W. Ashmanskas¹⁵ B. Auerbach⁵⁷ A. Aurisano⁴⁹ F. Azfar³⁹
W. Badgett¹⁵ T. Bae²⁵ A. Barbaro-Galtieri²⁶ V.E. Barnes⁴⁴ B.A. Barnett²³
P. Barria^{42,hh} P. Bartos¹² M. Baucé^{40,ff} F. Bedeschi⁴² S. Behari²³ G. Bellettini^{42,gg}
J. Bellinger⁵⁶ D. Benjamin¹⁴ A. Beretvas¹⁵ A. Bhatti⁴⁶ D. Bisello^{40,ff} I. Bizjak²⁸
K.R. Bland⁵ B. Blumenfeld²³ A. Bocci¹⁴ A. Bodek⁴⁵ D. Bortoletto⁴⁴ J. Boudreau⁴³
A. Boveia¹¹ L. Brigliadori^{6,ee} C. Bromberg³³ E. Brucken²¹ J. Budagov¹³ H.S. Budd⁴⁵
K. Burkett¹⁵ G. Busetto^{40,ff} P. Bussey¹⁹ A. Buzatu³¹ A. Calamba¹⁰ C. Calancha²⁹
S. Camarda⁴ M. Campanelli²⁸ M. Campbell³² F. Canelli^{11,15} B. Carls²² D. Carlsmith⁵⁶
R. Carosi⁴² S. Carrillo^{16,m} S. Carron¹⁵ B. Casal^{9,k} M. Casarsa⁵⁰ A. Castro^{6,ee}
P. Catastini¹⁹ D. Cauz⁵⁰ V. Cavaliere²² M. Cavalli-Sforza⁴ A. Cerri^{26,f} L. Cerrito^{28,s}
Y.C. Chen¹ M. Chertok⁷ G. Chiarelli⁴² G. Chlachidze¹⁵ F. Chlebana¹⁵ K. Cho²⁵
D. Chokheli¹³ W.H. Chung⁵⁶ Y.S. Chung⁴⁵ M.A. Ciocci^{42,hh} A. Clark¹⁸ C. Clarke⁵⁵
G. Compostella^{40,ff} M.E. Convery¹⁵ J. Conway⁷ M. Corbo¹⁵ M. Cordelli¹⁷ C.A. Cox⁷
D.J. Cox⁷ F. Crescioli^{42,gg} J. Cuevas^{9,z} R. Culbertson¹⁵ D. Dagenhart¹⁵
N. d'Ascenzo^{15,w} M. Datta¹⁵ P. de Barbaro⁴⁵ M. Dell'Orso^{42,gg} L. Demortier⁴⁶
M. Deninno⁶ F. Devoto²¹ M. d'Errico^{40,ff} A. Di Canto^{42,gg} B. Di Ruzza¹⁵
J.R. Dittmann⁵ M. D'Onofrio²⁷ S. Donati^{42,gg} P. Dong¹⁵ M. Dorigo⁵⁰ T. Dorigo⁴⁰
K. Ebina⁵⁴ A. Elagin⁴⁹ A. Eppig³² R. Erbacher⁷ S. Errede²² N. Ershaidat^{15,dd}
R. Eusebi⁴⁹ S. Farrington³⁹ M. Feindt²⁴ J.P. Fernandez²⁹ R. Field¹⁶ G. Flanagan^{15,u}
R. Forrest⁷ M.J. Frank⁵ M. Franklin¹⁹ J.C. Freeman¹⁵ Y. Funakoshi⁵⁴ I. Furic¹⁶
M. Gallinaro⁴⁶ J.E. Garcia¹⁸ A.F. Garfinkel⁴⁴ P. Garosi^{42,hh} H. Gerberich²²
E. Gerchtein¹⁵ S. Giagu⁴⁷ V. Giakoumopoulou³ P. Giannetti⁴² K. Gibson⁴³
C.M. Ginsburg¹⁵ N. Giokaris³ P. Giromini¹⁷ G. Giurgiu²³ V. Glagolev¹³ D. Glenzinski¹⁵
M. Gold³⁵ D. Goldin⁴⁹ N. Goldschmidt¹⁶ A. Golossanov¹⁵ G. Gomez⁹
G. Gomez-Ceballos³⁰ M. Goncharov³⁰ O. González²⁹ I. Gorelov³⁵ A.T. Goshaw¹⁴
K. Goulios⁴⁶ S. Grinstein⁴ C. Grosso-Pilcher¹¹ R.C. Group^{15,53}
J. Guimaraes da Costa¹⁹ S.R. Hahn¹⁵ E. Halkiadakis⁴⁸ A. Hamaguchi³⁸ J.Y. Han⁴⁵
F. Happacher¹⁷ K. Hara⁵¹ D. Hare⁴⁸ M. Hare⁵² R.F. Harr⁵⁵ K. Hatakeyama⁵
C. Hays³⁹ M. Heck²⁴ J. Heinrich⁴¹ M. Herndon⁵⁶ S. Hewamanage⁵ A. Hocker¹⁵
W. Hopkins^{15,g} D. Horn²⁴ S. Hou¹ R.E. Hughes³⁶ M. Hurwitz¹¹ U. Husemann⁵⁷
N. Hussain³¹ M. Hussein³³ J. Huston³³ G. Introzzi^{42,kk} M. Iori^{47,jj} A. Ivanov^{7,p}

E. James¹⁵ D. Jang¹⁰ B. Jayatilaka¹⁴ E.J. Jeon²⁵ S. Jindariani¹⁵ M. Jones⁴⁴
 K.K. Joo²⁵ S.Y. Jun¹⁰ T.R. Junk¹⁵ T. Kamon^{49,25} P.E. Karchin⁵⁵ A. Kasmi⁵
 Y. Kato^{38,o} W. Ketchum¹¹ J. Keung⁴¹ V. Khotilovich⁴⁹ B. Kilminster¹⁵ D.H. Kim²⁵
 H.S. Kim²⁵ J.E. Kim²⁵ M.J. Kim¹⁷ S.B. Kim²⁵ S.H. Kim⁵¹ Y.K. Kim¹¹ Y.J. Kim²⁵
 N. Kimura⁵⁴ M. Kirby¹⁵ S. Klimenko¹⁶ K. Knoepfel¹⁵ K. Kondo¹⁵⁴ D.J. Kong²⁵
 J. Konigsberg¹⁶ A.V. Kotwal¹⁴ M. Kreps²⁴ J. Kroll⁴¹ D. Krop¹¹ M. Kruse¹⁴
 V. Krutelyov^{49,c} T. Kuhr²⁴ M. Kurata⁵¹ S. Kwang¹¹ A.T. Laasanen⁴⁴ S. Lami^{42,gg,hh,ii}
 S. Lammel¹⁵ M. Lancaster²⁸ R.L. Lander⁷ K. Lannon^{36,y} A. Lath⁴⁸ G. Latino^{42,hh}
 T. LeCompte² E. Lee⁴⁹ H.S. Lee^{11,q} J.S. Lee²⁵ S.W. Lee^{49,bb} S. Leo^{42,gg} S. Leone⁴²
 J.D. Lewis¹⁵ A. Limosani^{14,t} C.-J. Lin²⁶ M. Lindgren¹⁵ E. Lipeles⁴¹ A. Lister¹⁸
 D.O. Litvintsev¹⁵ C. Liu⁴³ H. Liu⁵³ Q. Liu⁴⁴ T. Liu¹⁵ S. Lockwitz⁵⁷ A. Loginov⁵⁷
 D. Lucchesi^{40,ff} J. Lueck²⁴ P. Lujan²⁶ P. Lukens¹⁵ G. Lungu⁴⁶ J. Lys²⁶ R. Lysak^{12,e}
 R. Madrak¹⁵ K. Maeshima¹⁵ P. Maestro^{42,hh} S. Malik⁴⁶ G. Manca^{27,a}
 A. Manousakis-Katsikakis³ F. Margaroli⁴⁷ C. Marino²⁴ M. Martínez⁴ P. Mastrandrea⁴⁷
 K. Matera²² M.E. Mattson⁵⁵ A. Mazzacane¹⁵ P. Mazzanti⁶ K.S. McFarland⁴⁵
 P. McIntyre⁴⁹ R. McNulty^{27,j} A. Mehta²⁷ P. Mehtala²¹ C. Mesropian⁴⁶ T. Miao¹⁵
 D. Mietlicki³² A. Mitra¹ H. Miyake⁵¹ S. Moed¹⁵ N. Moggi⁶ M.N. Mondragon^{15,m}
 C.S. Moon²⁵ R. Moore¹⁵ M.J. Morello^{42,ii} J. Morlock²⁴ P. Movilla Fernandez¹⁵
 A. Mukherjee¹⁵ Th. Muller²⁴ P. Murat¹⁵ M. Mussini^{6,ee} J. Nachtman^{15,n} Y. Nagai⁵¹
 J. Naganoma⁵⁴ I. Nakano³⁷ A. Napier⁵² J. Nett⁴⁹ C. Neu⁵³ M.S. Neubauer²²
 J. Nielsen^{26,d} L. Nodulman² S.Y. Noh²⁵ O. Norniella²² L. Oakes³⁹ S.H. Oh¹⁴
 Y.D. Oh²⁵ I. Oksuzian⁵³ T. Okusawa³⁸ R. Orava²¹ L. Ortolan⁴ S. Pagan Griso^{40,ff}
 C. Pagliarone⁵⁰ E. Palencia^{9,f} V. Papadimitriou¹⁵ A.A. Paramonov² J. Patrick¹⁵
 G. Pauletta^{50,kk} M. Paulini¹⁰ C. Paus³⁰ D.E. Pellett⁷ A. Penzo⁵⁰ T.J. Phillips¹⁴
 G. Piacentino⁴² E. Pianori⁴¹ J. Pilot³⁶ K. Pitts²² C. Plager⁸ L. Pondrom⁵⁶
 S. Poprocki^{15,g} K. Potamianos⁴⁴ F. Prokoshin^{13,cc} A. Pranko²⁶ F. Ptohos^{17,h}
 G. Punzi^{42,gg} A. Rahaman⁴³ V. Ramakrishnan⁵⁶ N. Ranjan⁴⁴ I. Redondo²⁹ P. Renton³⁹
 M. Rescigno⁴⁷ T. Riddick²⁸ F. Rimondi^{6,ee} L. Ristori^{15,42} A. Robson¹⁹ T. Rodrigo⁹
 T. Rodriguez⁴¹ E. Rogers²² S. Rolli^{52,i} R. Roser¹⁵ F. Ruffini^{42,hh} A. Ruiz⁹ J. Russ¹⁰
 V. Rusu¹⁵ A. Safonov⁴⁹ W.K. Sakumoto⁴⁵ Y. Sakurai⁵⁴ L. Santi^{50,kk} K. Sato⁵¹
 V. Saveliev^{15,w} A. Savoy-Navarro^{15,aa} P. Schlabach¹⁵ A. Schmidt²⁴ E.E. Schmidt¹⁵
 T. Schwarz¹⁵ L. Scodellaro⁹ A. Scribano^{42,hh} F. Scuri⁴² S. Seidel³⁵ Y. Seiya³⁸
 A. Semenov¹³ F. Sforza^{42,hh} S.Z. Shalhout⁷ T. Shears²⁷ P.F. Shepard⁴³
 M. Shimojima^{51,v} M. Shochet¹¹ I. Shreyber-Tecker³⁴ A. Simonenko¹³ P. Sinervo³¹
 K. Sliwa⁵² J.R. Smith⁷ F.D. Snider¹⁵ A. Soha¹⁵ V. Sorin⁴ H. Song⁴³
 P. Squillacioti^{42,hh} M. Stancari¹⁵ R. St. Denis¹⁹ B. Stelzer³¹ O. Stelzer-Chilton³¹
 D. Stentz^{15,x} J. Strologas³⁵ G.L. Strycker³² Y. Sudo⁵¹ A. Sukhanov¹⁵ I. Suslov¹³
 K. Takemasa⁵¹ Y. Takeuchi⁵¹ J. Tang¹¹ M. Tecchio³² P.K. Teng¹ J. Thom^{15,g}
 J. Thome¹⁰ G.A. Thompson²² E. Thomson⁴¹ D. Toback⁴⁹ S. Tokar¹² K. Tollefson³³
 T. Tomura⁵¹ D. Tonelli¹⁵ S. Torre¹⁷ D. Torretta¹⁵ P. Totaro⁴⁰ M. Trovato^{42,ii}
 F. Ukegawa⁵¹ S. Uozumi²⁵ A. Varganov³² F. Vázquez^{16,m} G. Velez¹⁵ C. Vellidis¹⁵

¹Deceased

**M. Vidal⁴⁴ I. Vila⁹ R. Vilar⁹ J. Vizán⁹ M. Vogel³⁵ G. Volpi¹⁷ P. Wagner⁴¹
 R.L. Wagner¹⁵ T. Wakisaka³⁸ R. Wallny⁸ S.M. Wang¹ A. Warburton³¹ D. Waters²⁸
 W.C. Wester III¹⁵ D. Whiteson^{41,b} A.B. Wicklund² E. Wicklund¹⁵ S. Wilbur¹¹
 F. Wick²⁴ H.H. Williams⁴¹ J.S. Wilson³⁶ P. Wilson¹⁵ B.L. Winer³⁶ P. Wittich^{15,g}
 S. Wolbers¹⁵ H. Wolfe³⁶ T. Wright³² X. Wu¹⁸ Z. Wu⁵ K. Yamamoto³⁸ D. Yamato³⁸
 T. Yang¹⁵ U.K. Yang^{11,r} Y.C. Yang²⁵ W.-M. Yao²⁶ G.P. Yeh¹⁵ K. Yi^{15,n} J. Yoh¹⁵
 K. Yorita⁵⁴ T. Yoshida^{38,l} G.B. Yu¹⁴ I. Yu²⁵ S.S. Yu¹⁵ J.C. Yun¹⁵ A. Zanetti⁵⁰
 Y. Zeng¹⁴ C. Zhou¹⁴ S. Zucchelli^{6,ee}**

¹*Institute of Physics, Academia Sinica, Taipei, Taiwan 11529, Republic of China*

²*Argonne National Laboratory, Argonne, Illinois 60439, USA*

³*University of Athens, 157 71 Athens, Greece*

⁴*Institut de Física d'Altes Energies, ICREA, Universitat Autònoma de Barcelona, E-08193, Bellaterra (Barcelona), Spain*

⁵*Baylor University, Waco, Texas 76798, USA*

⁶*Istituto Nazionale di Fisica Nucleare Bologna, Italy*

⁷*University of California, Davis, Davis, California 95616, USA*

⁸*University of California, Los Angeles, Los Angeles, California 90024, USA*

⁹*Instituto de Física de Cantabria, CSIC-University of Cantabria, 39005 Santander, Spain*

¹⁰*Carnegie Mellon University, Pittsburgh, Pennsylvania 15213, USA*

¹¹*Enrico Fermi Institute, University of Chicago, Chicago, Illinois 60637, USA*

¹²*Comenius University, 842 48 Bratislava, Slovakia; Institute of Experimental Physics, 040 01 Kosice, Slovakia*

¹³*Joint Institute for Nuclear Research, RU-141980 Dubna, Russia*

¹⁴*Duke University, Durham, North Carolina 27708, USA*

¹⁵*Fermi National Accelerator Laboratory, Batavia, Illinois 60510, USA*

¹⁶*University of Florida, Gainesville, Florida 32611, USA*

¹⁷*Laboratori Nazionali di Frascati, Istituto Nazionale di Fisica Nucleare, I-00044 Frascati, Italy*

¹⁸*University of Geneva, CH-1211 Geneva 4, Switzerland*

¹⁹*Glasgow University, Glasgow G12 8QQ, United Kingdom*

²⁰*Harvard University, Cambridge, Massachusetts 02138, USA*

²¹*Division of High Energy Physics, Department of Physics, University of Helsinki and Helsinki Institute of Physics, FIN-00014, Helsinki, Finland*

²²*University of Illinois, Urbana, Illinois 61801, USA*

²³*The Johns Hopkins University, Baltimore, Maryland 21218, USA*

²⁴*Institut für Experimentelle Kernphysik, Karlsruhe Institute of Technology, D-76131 Karlsruhe, Germany*

²⁵*Center for High Energy Physics: Kyungpook National University, Daegu 702-701, Korea; Seoul National University, Seoul 151-742, Korea; Sungkyunkwan University, Suwon 440-746, Korea; Korea Institute of Science and Technology Information, Daejeon 305-806, Korea; Chonnam National University, Gwangju 500-757, Korea; Chonbuk National University, Jeonju 561-756, Korea*

²⁶*Ernest Orlando Lawrence Berkeley National Laboratory, Berkeley, California 94720, USA*

²⁷*University of Liverpool, Liverpool L69 7ZE, United Kingdom*

²⁸*University College London, London WC1E 6BT, United Kingdom*

²⁹*Centro de Investigaciones Energeticas Medioambientales y Tecnologicas, E-28040 Madrid, Spain*

- ³⁰ *Massachusetts Institute of Technology, Cambridge, Massachusetts 02139, USA*
- ³¹ *Institute of Particle Physics: McGill University, Montréal, Québec, Canada H3A 2T8; Simon Fraser University, Burnaby, British Columbia, Canada V5A 1S6; University of Toronto, Toronto, Ontario, Canada M5S 1A7; and TRIUMF, Vancouver, British Columbia, Canada V6T 2A3*
- ³² *University of Michigan, Ann Arbor, Michigan 48109, USA*
- ³³ *Michigan State University, East Lansing, Michigan 48824, USA*
- ³⁴ *Institution for Theoretical and Experimental Physics, ITEP, Moscow 117259, Russia*
- ³⁵ *University of New Mexico, Albuquerque, New Mexico 87131, USA*
- ³⁶ *The Ohio State University, Columbus, Ohio 43210, USA*
- ³⁷ *Okayama University, Okayama 700-8530, Japan*
- ³⁸ *Osaka City University, Osaka 588, Japan*
- ³⁹ *University of Oxford, Oxford OX1 3RH, United Kingdom*
- ⁴⁰ *Istituto Nazionale di Fisica Nucleare, Sezione di Padova-Trento, Italy*
- ⁴¹ *University of Pennsylvania, Philadelphia, Pennsylvania 19104, USA*
- ⁴² *Istituto Nazionale di Fisica Nucleare Pisa, Italy*
- ⁴³ *University of Pittsburgh, Pittsburgh, Pennsylvania 15260, USA*
- ⁴⁴ *Purdue University, West Lafayette, Indiana 47907, USA*
- ⁴⁵ *University of Rochester, Rochester, New York 14627, USA*
- ⁴⁶ *The Rockefeller University, New York, New York 10065, USA*
- ⁴⁷ *Istituto Nazionale di Fisica Nucleare, Sezione di Roma 1, Italy*
- ⁴⁸ *Rutgers University, Piscataway, New Jersey 08855, USA*
- ⁴⁹ *Texas A&M University, College Station, Texas 77843, USA*
- ⁵⁰ *Istituto Nazionale di Fisica Nucleare Trieste/Udine, I-34100 Trieste, Italy*
- ⁵¹ *University of Tsukuba, Tsukuba, Ibaraki 305, Japan*
- ⁵² *Tufts University, Medford, Massachusetts 02155, USA*
- ⁵³ *University of Virginia, Charlottesville, Virginia 22906, USA*
- ⁵⁴ *Waseda University, Tokyo 169, Japan*
- ⁵⁵ *Wayne State University, Detroit, Michigan 48201, USA*
- ⁵⁶ *University of Wisconsin, Madison, Wisconsin 53706, USA*
- ⁵⁷ *Yale University, New Haven, Connecticut 06520, USA*

With visitors from

- ^a *Istituto Nazionale di Fisica Nucleare, Sezione di Cagliari, 09042 Monserrato (Cagliari), Italy*
- ^b *University of CA Irvine, Irvine, CA 92697, USA*
- ^c *University of CA Santa Barbara, Santa Barbara, CA 93106, USA*
- ^d *University of CA Santa Cruz, Santa Cruz, CA 95064, USA*
- ^e *Institute of Physics, Academy of Sciences of the Czech Republic, Czech Republic*
- ^f *CERN, CH-1211 Geneva, Switzerland*
- ^g *Cornell University, Ithaca, NY 14853, USA*
- ^h *University of Cyprus, Nicosia CY-1678, Cyprus*
- ⁱ *Office of Science, U.S. Department of Energy, Washington, DC 20585, USA*
- ^j *University College Dublin, Dublin 4, Ireland*
- ^k *ETH, 8092 Zurich, Switzerland*

- ^l *University of Fukui, Fukui City, Fukui Prefecture, Japan 910-0017*
- ^m *Universidad Iberoamericana, Mexico D.F., Mexico*
- ⁿ *University of Iowa, Iowa City, IA 52242, USA*
- ^o *Kinki University, Higashi-Osaka City, Japan 577-8502*
- ^p *Kansas State University, Manhattan, KS 66506, USA*
- ^q *Ewha Womans University, Seoul, 120-750, Korea*
- ^r *University of Manchester, Manchester M13 9PL, United Kingdom*
- ^s *Queen Mary, University of London, London, E1 4NS, United Kingdom*
- ^t *University of Melbourne, Victoria 3010, Australia*
- ^u *Muons, Inc., Batavia, IL 60510, USA*
- ^v *Nagasaki Institute of Applied Science, Nagasaki, Japan*
- ^w *National Research Nuclear University, Moscow, Russia*
- ^x *Northwestern University, Evanston, IL 60208, USA*
- ^y *University of Notre Dame, Notre Dame, IN 46556, USA*
- ^z *Universidad de Oviedo, E-33007 Oviedo, Spain*
- ^{aa} *CNRS-IN2P3, Paris, F-75205 France*
- ^{bb} *Texas Tech University, Lubbock, TX 79609, USA*
- ^{cc} *Universidad Tecnica Federico Santa Maria, 110v Valparaiso, Chile*
- ^{dd} *Yarmouk University, Irbid 211-63, Jordan*
- ^{ee} *University of Bologna, I-40127 Bologna, Italy*
- ^{ff} *University of Padova, I-35131 Padova, Italy*
- ^{gg} *University of Pisa*
- ^{hh} *University of Siena*
- ⁱⁱ *Scuola Normale Superiore, I-56127 Pisa, Italy*
- ^{jj} *California Institute of Technology, Pasadena, California 91125, USA*
- ^{kk} *INFN Pavia and University of Pavia, Italy*

ABSTRACT:

This paper reports the result of a search for the standard model Higgs boson in events containing four reconstructed jets associated with quarks. For masses below $135 \text{ GeV}/c^2$, the Higgs boson decays to bottom-antibottom quark pairs are dominant and result primarily in two hadronic jets. An additional two jets can be produced in the hadronic decay of a W or Z boson produced in association with the Higgs boson, or from the incoming quarks that produced the Higgs boson through the vector-boson fusion process. The search is performed using a sample of $\sqrt{s} = 1.96 \text{ TeV}$ proton-antiproton collisions corresponding to an integrated luminosity of 9.45 fb^{-1} recorded by the CDF II detector. The data are in agreement with the background model and 95% credibility level upper limits on Higgs boson production are set as a function of the Higgs boson mass. The median expected (observed) limit for a $125 \text{ GeV}/c^2$ Higgs boson is 11.0 (9.0) times the predicted standard model rate.

KEYWORDS: Higgs, All-Hadronic, b -jets

Contents

1	Introduction	1
2	The CDF II detector	2
3	Event selection	3
4	Signal and background samples	4
5	Search strategy	5
6	QCD multi-jet background prediction	6
7	Energy correction for b jets	7
8	Untagged jets neural network	8
9	Jet width	9
10	Classification of Higgs boson events	10
11	Systematic uncertainties	17
12	Results	19
13	Summary	19

1 Introduction

The Higgs boson is the physical manifestation of the hypothesized mechanism that provides mass to fundamental particles in the standard model (SM) [1–3]. Direct searches at the LEP collider [4], the Tevatron [5], and the LHC [6, 7] have excluded SM Higgs boson masses at the 95% confidence level or 95% credibility level (CL), except within the range 122-128 GeV/ c^2 . The most sensitive searches at the LHC are based on SM Higgs boson decays to pairs of gauge bosons. At the Tevatron, searches based on Higgs boson decay to bottom-antibottom quark pairs ($b\bar{b}$) are the most sensitive within the allowed range. Searches in this channel offers complementary information on fermion Yukawa couplings to the Higgs boson.

Recently, the ATLAS and CMS collaborations have reported the observation of a Higgs-like particle at a mass of ≈ 125 GeV/ c^2 [6, 7], and the Tevatron has reported evidence for a particle decaying to $b\bar{b}$ produced in association with a W/Z boson for masses within the range 120 - 135 GeV/ c^2 [8].

This paper describes a search for the Higgs boson using a data sample corresponding to an integrated luminosity of 9.45 fb^{-1} of $p\bar{p}$ collisions at $\sqrt{s} = 1.96 \text{ TeV}$ recorded by the Collider Detector at Fermilab (CDF II). In this search two production mechanisms are studied: associated vector-boson production (VH) and vector-boson fusion (VBF). The VH channel denotes the process $p\bar{p} \rightarrow W/Z + H \rightarrow q\bar{q}' + b\bar{b}$. The VBF channel identifies the process $p\bar{p} \rightarrow q\bar{q}'H \rightarrow q\bar{q}'b\bar{b}$, where the two incoming quarks each radiate a weak boson, which subsequently fuse into a Higgs boson. In both channels, the Higgs boson decays to $b\bar{b}$, and is produced in association with two other quarks ($q\bar{q}'$). Data are tested against the hypothesis of the presence of Higgs boson with mass in the range $100 < m_H < 150 \text{ GeV}/c^2$. The $H \rightarrow b\bar{b}$ mode is the dominant decay for $m_H < 135 \text{ GeV}/c^2$ [9].

Searches for a Higgs boson performed in final states containing leptons, jets, and missing energy have the advantage of smaller background, but the Higgs boson signal yields are also very small. The all-hadronic search channel, described here, has larger potential signal contributions but suffers from substantial QCD multi-jet background contributions. The challenge of this channel is to accurately model and reduce the multi-jet background. Two previous papers were published on searches for a Higgs boson in the all-hadronic channel at CDF using data sets of 2 fb^{-1} [10] and 4 fb^{-1} [11]. Another paper was published on searches for a Higgs boson in the all-hadronic channel at CDF using data collected during Run I [12]. The LEP collider also conducted searches for the Higgs boson in the all-hadronic final state in the $e^+e^- \rightarrow ZH \rightarrow q\bar{q} + b\bar{b}$ channel [4].

2 The CDF II detector

The CDF II detector is an azimuthally and forward-backward symmetric multipurpose detector. CDF II uses a cylindrical coordinate system with the z -axis aligned along the proton beam direction, where θ is the polar angle relative to the z -axis and ϕ is the azimuthal angle relative to the x -axis. The pseudorapidity is defined as $\eta = -\ln(\tan \theta/2)$ and the transverse energy is calculated as $E_T = E \sin \theta$.

The CDF II detector consists of a pair of concentric charged-particle tracking detectors immersed in a 1.4 T solenoid magnetic field, surrounded by calorimeters and muon detectors. The inner tracking detector is the silicon vertex detector that is located immediately outside the beam pipe, provides precise three-dimensional reconstruction of charged-particle trajectories (tracks) and is used to identify displaced vertices associated with bottom-quark and charm-quark hadron decays. The momenta of charged particles is measured precisely in the central outer tracker (COT), a cylindrical multiwire drift chamber. The tracking detectors cover the pseudorapidity range $|\eta| < 1.1$. Outside the COT are electromagnetic and hadronic calorimeters arranged in a projective-tower geometry, covering the region $|\eta| < 3.5$, to provide energy measurements for both charged and neutral particles. Drift chambers and scintillator counters in the region $|\eta| < 1.5$ provide muon identification outside the calorimeters. Luminosity is measured using low-mass gaseous Cherenkov luminosity counters (CLC). There are two CLC modules in the CDF II detector installed at small angles in the proton and antiproton directions, arranged in three

concentric layers around the beam pipe. More details about the CDF II detector can be found in refs. [13–15].

Jets are defined by a cluster of energy deposited in the calorimeter using a jet clustering algorithm (JetClu) [16] with a cone of fixed radius. The JetClu algorithm begins by creating a list of calorimeter towers above a fixed E_T threshold to be used as seeds for the jet finder. This threshold is set to 1.0 GeV. Preclusters are formed from an unbroken chain of contiguous seed towers with a continuously decreasing tower E_T . If a tower is outside a window of seven towers surrounding the seed, it is used to form a new precluster. These preclusters are used as a starting point for cone clustering. First, the E_T weighted centroid of the precluster is found and a cone in $\eta - \phi$ space of radius R is formed around the centroid. For this analysis, $\Delta R = \sqrt{(\Delta\phi)^2 + (\Delta\eta)^2} = 0.4$. Then, all towers with an E_T of, at least, 100 MeV are incorporated into the cluster. A tower is included in a cluster if its centroid is inside the cone, otherwise it is excluded. A new cluster center is calculated from the set of towers within the clustering cone, again using an E_T weighted centroid, and a new cone is drawn about this position. The process of recomputing a centroid and finding new or deleting old towers is iterated until the tower list remains unchanged. Corrections are applied to the measured jet energy to account for detector calibrations, multiple interactions, underlying event, and energy outside of the jet cone [17].

The data for this analysis are collected using two online event selections (triggers). Events in the first 3.0 fb^{-1} are triggered by selecting those containing at least four jets with $E_T \geq 15 \text{ GeV}$ and total calorimeter E_T greater than 175 GeV. Events in the remaining 6.45 fb^{-1} are selected by requiring at least three jets with $E_T \geq 20 \text{ GeV}$ and total calorimeter E_T greater than 130 GeV.

3 Event selection

Events with isolated leptons or missing transverse energy significance¹ greater than 6.0, which is indicative of the presence of neutrinos, are removed to ensure an event sample independent from other Higgs boson searches at CDF. Events containing four or five jets, with $E_T > 15 \text{ GeV}$ and $|\eta| < 2.4$ are selected.

To reduce the QCD multi-jet background, exactly two bottom-quark jets (b jets) are required. Two algorithms are used to identify b jets: the SecVtx algorithm [14] and the JetProb algorithm [18]. The SecVtx algorithm attempts to reconstruct the secondary vertex associated with a bottom-quark (b) decay. The JetProb algorithm searches the impact parameter of the charged-particle trajectories (tracks) within a jet and selects those that are inconsistent with originating from the decay of a particle occurred in the vicinity of the primary event vertex. An additional energy correction is applied to jets identified as b jets (section 7). Untagged jets (non b jets) are referred to as q jets in this paper.

¹Missing transverse energy significance is defined as the ratio of the missing transverse energy to the square root of the total transverse energy. The missing transverse energy, $\cancel{E}_T = |\vec{\cancel{E}}_T|$, where $\vec{\cancel{E}}_T$ is defined by, $\vec{\cancel{E}}_T = -\sum_i E_T^i \hat{n}_i$, where i is calorimeter tower number with $|\eta| < 3.6$, \hat{n}_i is a unit vector perpendicular to the beam axis and pointing at the i^{th} calorimeter tower.

All selected jets are ordered in E_T and the four highest E_T jets are considered. The scalar sum of the four selected jet E_T s (SumEt) is required to exceed 220 GeV and two of the four selected jets must be b jets.

The signal-to-background ratio is enhanced by dividing the data into two independent b -tagging categories: SS in which both jets are tagged by SecVtx, and SJ in which one jet is tagged by SecVtx and the other by JetProb. If a jet is tagged by both algorithms, it is classified as tagged by SecVtx because of the lower misidentification rate. Events in which both jets are tagged only by JetProb are not used because the increase in background contributions is substantially larger than that for the signal.

The signal region is defined by requirements on the invariant mass of the two b -tagged jets (m_{bb}) and the two untagged jets (m_{qq}). The VH channel features two intermediate resonances, one from the potential Higgs boson decay, in m_{bb} , and another from the W/Z decay, in m_{qq} . The VBF channel shares the same m_{bb} resonance but the two q jets are not produced from the decay of a particle. However these two q jets tend to be produced with large η separation which gives a large effective m_{qq} mass. The Higgs boson search region is defined as $75 < m_{bb} < 175 \text{ GeV}/c^2$ and $m_{qq} > 50 \text{ GeV}/c^2$.

4 Signal and background samples

Backgrounds that contribute to the $qqb\bar{b}$ final state originate from QCD multi-jet production, top-quark pair production, single-top-quark production, $W \rightarrow q'\bar{q}$ plus $b\bar{b}$ or charm-quark pair ($c\bar{c}$) production ($W+HF$), $Z \rightarrow b\bar{b}, c\bar{c}$ plus jets production ($Z+\text{jets}$), and diboson production (WW, WZ, ZZ). About 98% of the total background comes from QCD multi-jet production. Signal and non-QCD backgrounds yields are estimated from Monte Carlo (MC) simulation. The $W+HF$ and $Z+\text{jets}$ contributions are modeled with the ALPGEN [19] generator for simulating the bosons plus parton production, and PYTHIA [20] for modeling parton showers. The other non-QCD backgrounds and the signal are modeled with PYTHIA [20]. All MC-simulated samples use the CTEQ5L [21] parton distribution function (PDF) at leading order (LO) and are processed through the full CDF II detector simulation [22], based on GEANT [23], that includes the trigger simulation and their trigger efficiencies are corrected as described in ref. [10].

The expected signal yield in the SS (SJ) channel is 27.1 ± 4.1 (9.1 ± 1.4) for $m_H = 125 \text{ GeV}/c^2$. The selected number of data events for SS (SJ) are 87272 (46818). A data-driven model is used to predict the shape of QCD multi-jet background but not the overall yield (section 6). The number of QCD multi-jet events in each channel is estimated as the difference between the number of data events and the predicted number of non-QCD events estimated with MC (neglecting the potential Higgs boson contribution). Expected and observed event yields are summarized in table 1. In the final fit used to extract a potential Higgs boson signal, the overall normalization of the QCD multi-jet background is treated as an unconstrained parameter.

Backgrounds	SS channel	SJ channel
$t\bar{t}$	1032 ± 156	384 ± 57
Single top s channel	111 ± 19	38 ± 6
Single top t channel	44 ± 7	26 ± 4
$W + b\bar{b}$	77 ± 40	29 ± 15
$W + c\bar{c}$	8 ± 4	7 ± 4
$Z(\rightarrow b\bar{b}/c\bar{c})+\text{jets}$	873 ± 452	338 ± 175
WW	6 ± 1	6 ± 1
WZ	20 ± 3	8 ± 1
ZZ	21 ± 3	8 ± 1
Total non-QCD	2192 ± 480	844 ± 185
Data	87272	46818
QCD multi-jet	85080	45974
Higgs signal ($125 \text{ GeV}/c^2$)	27 ± 4	9 ± 1

Table 1. Expected number of background and signal ($m_H = 125 \text{ GeV}/c^2$) events that pass the complete event selection for the SS and SJ b -tag categories. The number of QCD multi-jet events is estimated as the difference between data and predicted non-QCD backgrounds (neglecting the potential Higgs contribution). The uncertainties of the signal and non-QCD background rate predictions include statistical and systematic rate uncertainties, such as cross-section and integrated luminosity, as described in section 11.

5 Search strategy

The main challenge is to accurately model and reduce the QCD multi-jet background. The modeling of this background is obtained from a data-driven technique described in section 6. This avoids the need of generating large volumes of QCD multi-jet simulation samples, which is computationally intensive and unlikely to accurately reproduce the multi-jet spectrum.

The overwhelming QCD multi-jet background is suppressed by relying on multi-variate techniques that combine information from multiple variables to identify potential Higgs boson events. For example, the best signal-to-background ratio using just m_{bb} is 0.0007². In this search, the use of multi-variate techniques improves the signal-to-background to 0.006³, a factor of 10 improvement. A total of eleven artificial neural networks (NN) [24, 25] are used to improve the resolutions of variables sensitive to Higgs production and to separate the signal and background contributions. Altogether, the use of these NN leads to a 24% increase in search sensitivity⁴, in addition to that expected from the inclusion of additional data with respect to the previous analysis [11].

This analysis focuses on Higgs boson decays to $b\bar{b}$, and thus it is important to have the best possible resolution for m_{bb} . Section 7 describes a NN used to correct the energies of

²Only considering events under the Higgs signal peak ($120 < m_{bb} < 140 \text{ GeV}/c^2$), figure 3(a).

³Only considering events with Higgs-NN > 0.95 , figure 8.

⁴The search sensitivity is defined as the percentage reduction of the median expected limit.

b jets, which in turn improves m_{bb} . The untagged jets (q jets) associated with each Higgs production process have unique angular and kinematic distributions. Section 8 describes three networks that exploit these variables to identify q jets from Higgs boson events. As gluon jets are typically wider than quark jets, jet width is useful for separating events containing quark jets associated with Higgs-boson production from generic jets contained within QCD multi-jet events, which are a mixture of quark and gluon jets. Section 9 describes a technique for measuring jet width and a NN used to remove detector and kinematic dependences that also influence the jet width.

Section 10 describes the final two-stage NN that is used to extract a potential signal contribution from the backgrounds. The two-stage NN can identify Higgs bosons produced by three different processes simultaneously. The first stage is based on three separate NNs trained specifically to separate backgrounds from either WH , ZH , or VBF Higgs production, respectively, to exploit the unique characteristics of each signal process. The outputs of the three process-specific NNs are used as inputs to a second NN. The inputs to the first-stage networks are the corrected b -jet energies, corrected q -jet widths, outputs of the q -jet networks, and other kinematic event variables. In the previous search [11], exclusive VH and VBF networks were used to search for Higgs bosons in non-overlapping signal regions. The two-stage NN, developed for this search, increases the search sensitivity by 15%. The use of a single signal region increases the number of potential Higgs boson signal events by 20%. Both gains are above those expected from the inclusion of additional data alone.

6 QCD multi-jet background prediction

Kinematic features of the QCD multi-jet background are predicted using a data-driven method. An independent data control region is used to measure the probability for an event with one b -tagged jet to contain an additional b -tagged jet (probe jet), referred to as the Tag Rate Function (TRF). The TRF is applied to data samples with exactly one jet b -tagged by SecVtx to predict the distribution of events with two b -tagged jets. The TRF is parameterized as a function of three variables: E_T of the probe jet, η of the probe jet, and ΔR between the tagged b jet and probe jet, and implemented as a three-dimensional histogram. The choice of variables used to parameterize the TRF is motivated by the kinematics of the QCD multi-jet background and the characteristics of the b -tagging algorithms. For example, the production of b jets from gluon splitting has a different ΔR distribution compared to direct production, and the probe jet E_T and η expresses aspects of the b -tagging algorithms and QCD multi-jet production. Further information on the technique can be found in [10].

We use separate TRFs for SS and SJ events, which are obtained from events in the TAG region (figure 1), defined as $m_{qq} \in [40 \text{ GeV}/c^2, 45 \text{ GeV}/c^2] \cup m_{bb} \in [65 \text{ GeV}/c^2, 250 \text{ GeV}/c^2]$ and $m_{qq} > 45 \text{ GeV}/c^2 \cup m_{bb} \in [65 \text{ GeV}/c^2, 70 \text{ GeV}/c^2] \cup m_{bb} \in [200 \text{ GeV}/c^2, 250 \text{ GeV}/c^2]$. To validate the background model, the TRF is tested in the TAG (for self-consistency) and two other control regions non-overlapping with the signal region (figure 1): the CONTROL region, defined as $m_{qq} \in [45 \text{ GeV}/c^2, 50 \text{ GeV}/c^2] \cup m_{bb} \in [70 \text{ GeV}/c^2, 200 \text{ GeV}/c^2]$ and $m_{qq} > 50 \text{ GeV}/c^2 \cup m_{bb} \in [70 \text{ GeV}/c^2, 75 \text{ GeV}/c^2] \cup m_{bb} \in [175 \text{ GeV}/c^2, 200 \text{ GeV}/c^2]$; and

the NJET6 control region defined as sharing the same m_{bb} and m_{qq} criteria as the signal region, but contains those events with six reconstructed jets. The TRF prediction of different variables are compared to data in these control regions and any shape difference is propagated as an uncertainty of the QCD multi-jet model.

The m_{qq} variable is not perfectly modeled by the TRF. The residual mismodeling is corrected by following the procedure defined in previous searches [10, 11], which reweights events as a function of the observed m_{qq} . The correction function is derived from a fit to the ratio of the observed m_{qq} over the same quantity predicted by TRF in events from the TAG region.

Figures 3-6 show a comparison of observed data and background predictions in the signal region for the variables used in the final signal discrimination neural network (section 10) after application of the m_{qq} correction function. The modeling of some variables appears to be poor but the differences are within the shape uncertainties of the QCD multi-jet prediction. More details on these variables are given in the following sections.

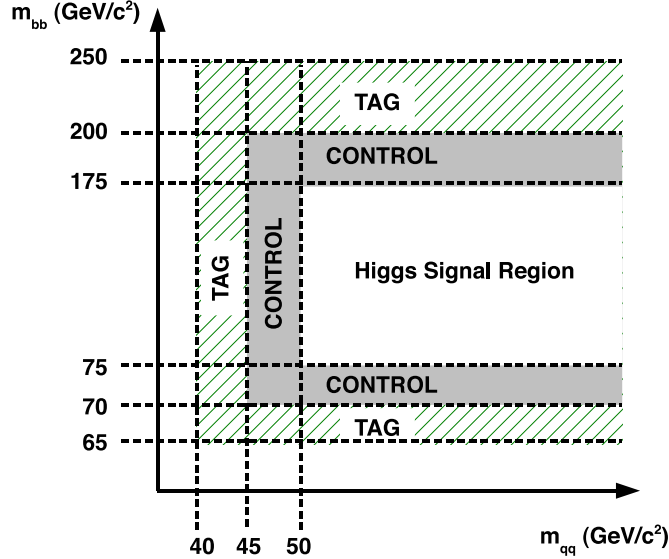


Figure 1. Signal and controls regions in the m_{bb} - m_{qq} plane. The TAG region is used to derive the TRF for modeling the QCD multi-jet background. The CONTROL region is used to test and derive systematic uncertainties of this background model.

7 Energy correction for b jets

The experimental resolution of the invariant mass of the two b jets, m_{bb} , has a significant effect on the sensitivity of our search. To improve the m_{bb} resolution, a NN is trained to estimate the correction factor required to obtain the best possible estimate of the parent b -parton energy from the measured jet energy [26].

A NN is trained for each b -tagging algorithm. Nine variables, describing a given jet, are used to train the NN for SecVtx tagged jets. These are the jet E_T , the jet transverse

momentum ($p_T \equiv p \sin \theta$), the E_T before the application of jet energy correction (uncorrected jet E_T), the transverse mass⁵, the decay length of the jet in the transverse plane⁶ and its uncertainty, the p_T of the secondary vertex, the maximum p_T of the tracks inside the jet cone, and the p_T sum of all tracks within the jet cone. Six variables are used to train the NN for JetProb tagged jets: the jet E_T , the jet p_T , the uncorrected jet E_T , the transverse mass, the maximum p_T of the tracks inside the jet cone, and the p_T sum of all tracks within the jet cone.

The NNs are trained using simulated VBF events⁷ with Higgs masses from 100 GeV/ c^2 to 150 GeV/ c^2 at 5 GeV/ c^2 intervals. Events are required to pass the selection described in section 3 and each b -tagged jet is required to be matched geometrically with a b parton. The matching criterion requires the ΔR between the b jet and b parton not to exceed 0.4. SecVtx- and JetProb-tagged jets are used to train the SecVtx and JetProb networks, respectively.

Figure 2 shows the m_{bb} distribution in simulated decays of 125 GeV/ c^2 Higgs bosons produced through VBF, before and after b -jet energies are corrected. The mean shifts from 116 GeV/ c^2 to 128 GeV/ c^2 and the root mean square (RMS) from 15.6 GeV/ c^2 to 13.7 GeV/ c^2 . The resolution, defined as the ratio between the RMS and the mean, shifts from 0.13 to 0.11, an improvement of 18%.

The b -jet energy corrections should be independent of the sample used to train and test the NN. The NN training and testing was repeated using WH and ZH events and similar results were obtained.

8 Untagged jets neural network

The angular distributions of untagged jets (q jets) from VH or VBF differs from the angular distributions of generic jets contained within QCD multi-jet background events. Identification of q jets can therefore help to separate signal events from QCD multi-jet background contributions. In particular, the m_{qq} obtained from q jets associated with the WH and ZH processes is constrained by the mass of the W and Z , respectively. The q jets produced in VBF events are typically separated by large ϕ and η , while the q jets in QCD multi-jet events tend to exhibit a large difference in ϕ and a small difference in η . Three networks [24], referred to as $qq\text{-}WH$ NN, $qq\text{-}ZH$ NN, and $qq\text{-}VBF$ NN, are trained to separate events with q jets originating from WH , ZH , and VBF production from background events. The input variables are m_{qq} , $\Delta\phi_{qq}$, $\Delta\eta_{qq}$, ΔR_{qq} , and the transverse momenta of each q jet with respect to the total momentum of the system. The networks are trained using Higgs MC to model signal and data-driven prediction for QCD multi-jets to model background. Examples of the output distributions of these trained neural network are shown in figure 7.

⁵The transverse mass is defined as $(p_T/p)M$, where M is the invariant mass of the jet.

⁶The decay length is defined as the transverse distance between the primary vertex and the reconstructed secondary vertex in the SecVtx b -tagged jet.

⁷All NNs in this paper are trained using statistically independent samples.

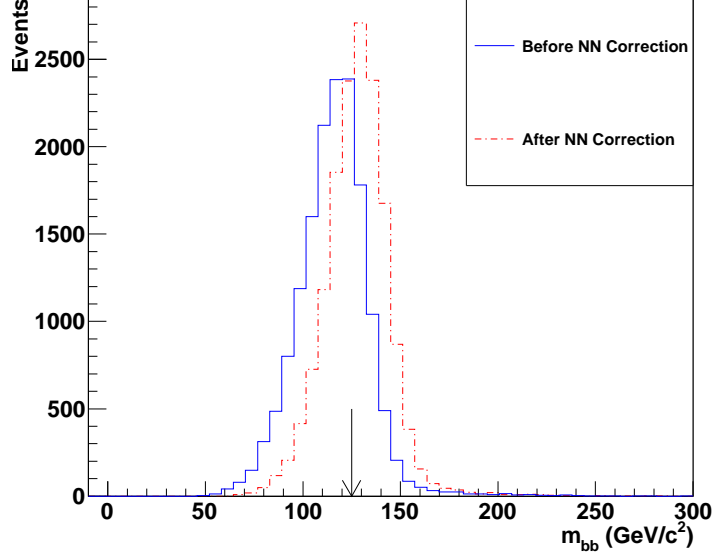


Figure 2. Comparison of m_{bb} distribution in simulated decays of $125 \text{ GeV}/c^2$ Higgs bosons produced through VBF, before and after the b -jet energy correction for a VBF MC sample with $m_H = 125 \text{ GeV}/c^2$ (indicated by the black arrow).

9 Jet width

The untagged jets (q jets) associated with the QCD multi-jet background are a mixture of quark and gluon jets whereas the q jets associated with the Higgs signal are predominantly quark jets. As gluon jets tend to be broader than quark jets, jet width is another useful variable for distinguishing potential Higgs events from the background. We defined jet widths measured within the calorimeter ($\langle R \rangle_{\text{CAL}}$) and tracker ($\langle R \rangle_{\text{TRK}}$) as

$$\langle R \rangle_{\text{CAL}} = \sqrt{\sum_{\text{towers}} \left[\frac{E_t^{\text{tower}}}{E_t^{\text{jet}}} \left(\Delta R(\text{tower}, \text{jet}) \right)^2 \right]} \quad (9.1)$$

$$\langle R \rangle_{\text{TRK}} = \sqrt{\sum_{\text{tracks}} \left[\frac{P_t^{\text{track}}}{P_t^{\text{jet}}} \left(\Delta R(\text{track}, \text{jet}) \right)^2 \right]}, \quad (9.2)$$

where $\Delta R(\text{tower}, \text{jet})$ ($\Delta R(\text{track}, \text{jet})$) is the angular distance between the jet axis and the calorimeter tower (track). All calorimeter towers within the jet cone of $\Delta R < 0.4$ are used in the $\langle R \rangle_{\text{CAL}}$ calculation. All tracks with $p_T > 1 \text{ GeV}/c$ and within the jet cone of $\Delta R < 0.4$ are used in the calculation of $\langle R \rangle_{\text{TRK}}$.

The jet width also varies as a function of jet E_T , jet η , and the number of primary vertices (N_{vtx}), and is parameterized by a neural network fit. These dependences are removed by rescaling the measured jet widths to a common reference (that for a jet with $E_T=50 \text{ GeV}$, $\eta=0$, and $N_{\text{vtx}}=1$) using the procedure described in ref. [11]. The NN function

to parameterize the variation of jet width with jet E_T , jet η , and N_{vtx} , is trained on a sample of untagged quark jets from the hadronic W boson decays in $t\bar{t} \rightarrow b\bar{b}l\nu qq$ ($\ell = e, \mu$) events. The highest E_T untagged-jet pair whose invariant mass is in the range $50 - 110 \text{ GeV}/c^2$ is assumed to originate from the hadronic W boson decay. Separate networks are trained for MC and data. After rescaling, any differences in the jet width are assumed to be associated with the type of parton that initiated the jet. The $t\bar{t}$ MC and data q -jet width distributions are found to agree after rescaling the measured jet widths. To check that the jet width rescaling can be applied to non- $t\bar{t}$ samples, the rescaling is also applied to the q jets in WH , ZH , and VBF MC events. The mean rescaled jet width in all samples is consistent with the width observed in the $t\bar{t}$ sample, which verifies the independence of the corrections with respect to jet E_T , η , and N_{vtx} .

A systematic uncertainty is assigned by adding an offset to the rescaled $t\bar{t}$ MC jet width and comparing the $\chi^2/\text{degree of freedom}$ ($\chi^2/\text{d.o.f}$) of the shifted MC and $t\bar{t}$ data distributions with the unshifted MC and data. The uncertainty is defined by the offset that changes the $\chi^2/\text{d.o.f}$ by ± 1 unit. The calorimeter jet width uncertainty is $\pm 2.6\%$ and the tracker jet width uncertainty is $\pm 5.5\%$.

Figures 4(c)-4(f) show the corrected jet width distributions of the untagged jets measured by the calorimeter and tracker. The Higgs signal tends to lower jet width values, which implies quark-like, whereas the QCD multi-jet tends to higher jet width, which implies a mixture of quark and gluons. The jet width distributions of the Higgs signal is different to the background which shows this variable is useful for the Higgs boson search.

10 Classification of Higgs boson events

A final NN is trained to optimize the separation of signal and background [24], which incorporates information from kinematic and angular jet variables, jet widths, event shapes, and the outputs of the untagged jets (q jets) NNs. The energies of the b jets and widths of the q jets are corrected as described in sections 7 and 9, respectively. As the WH , ZH , and VBF processes have different kinematics, dedicated WH , ZH , and VBF networks are trained separately for each process, resulting in three outputs. The outputs of the process-specific NNs are combined as inputs to a grand NN, referred to as the Higgs-NN. The output of the Higgs-NN is used to obtain Higgs search limits.

The selection of input variables for the process specific WH , ZH , and VBF networks training must fulfill two criteria: the variables must have good background-to-signal separation, and they must be well modeled by TRF. The discriminating variables for the WH -NN and ZH -NN training are m_{bb} , m_{qq} , the cosine of the leading-jet scattering angle in the four-jet rest-frame ($\cos(\theta_3)$) [27], the χ variable⁸ [11], the calorimeter jet width of the first ($\langle R \rangle_{CAL}^{q1}$) and second leading untagged jet ($\langle R \rangle_{CAL}^{q2}$), the tracker jet width of the first ($\langle R \rangle_{TRK}^{q1}$) and second leading untagged jet ($\langle R \rangle_{TRK}^{q2}$), aplanarity⁹, sphericity¹⁰, cen-

⁸ χ variable is the minimum of χ_W and χ_Z where $\chi_W = \sqrt{(M_W - m_{qq})^2 + (M_H - m_{bb})^2}$ and a similar expression exists for χ_Z .

⁹Aplanarity measures the transverse momentum component out of the event plane.

¹⁰Sphericity is a measure of the summed transverse momentum squared with respect to the event axis.

trality¹¹ [20], ΔR of the two b -tagged jets, ΔR of the two untagged jets, $\Delta\phi$ of the two b -tagged jets, $\Delta\phi$ of the two untagged jets, and the $qq\text{-}WH$ and $qq\text{-}ZH$ network outputs (section 8). Not all variables used in the WH and ZH networks' training have a good background-to-signal separation for VBF. For the VBF-NN training, the $\cos(\theta_3)$, the aplanarity, and the $\Delta\phi$ of the two untagged jets are removed; the η angle of the first (η_{q_1}) and second leading untagged jet (η_{q_2}), the $\Delta\eta$ of the two untagged jets ($\Delta\eta_{qq}$), the invariant mass of four jets system, the sum of the four jets' momenta along z direction are added, and the $qq\text{-}WH$ and $qq\text{-}ZH$ network outputs are replaced by $qq\text{-}VBF$ NN output. Overall, the $VH(VBF)\text{-}NN$ is trained with 17(18) variables, of which m_{bb} and m_{qq} (m_{qq} and $\Delta\eta_{qq}$) are the most discriminating variables.

The distributions of the discriminating variables for the Higgs signal and background are shown in figures 3-7. The presence of a resonance in the VH and VBF channels, due to the potential Higgs boson decay, produces a peak in the m_{bb} that is not present in the QCD multi-jet background (figure 3(a)). A similar observation can be made for the m_{qq} distribution in figure 3(b), where the VH channel features a resonance due to the W/Z decay (not observed in the VBF channel since the two q jets are not produced from the decay of a particle). In figures 4(c)-(f) the jet width distributions of untagged jets of the QCD multi-jet background are broader than the Higgs signal due to the reason that is described in section 9. The two q jets produced in the VBF events, which are produced from the two incoming quarks that each radiates a weak boson, tend to point in the forward but opposite directions. Thus the two q jets are widely separated in the pseudo rapidity space. These features are shown in figures 5(a)-(c). The $qq\text{-}WH$ NN (figure 7(a)), $qq\text{-}ZH$ NN (figure 7(b)), and $qq\text{-}VBF$ NN (figure 7(c)) distributions are the outputs of three neural networks that are trained to separate the QCD multi-jet events from WH , ZH and VBF productions, respectively.

Each variable demonstrates some ability to distinguish a Higgs boson from the background. Some variables, such as figures 3(c) and 7(a) appear to have some mismodeling of the background. However the observed difference are within the shape uncertainties of the TRF QCD multi-jet prediction. These shape uncertainties are derived by testing these variables in the TAG, CONTROL, and NJET6 control regions and propagating any difference as a shape uncertainty.

¹¹Centrality measures how much of the energy flows into the central rapidity region.

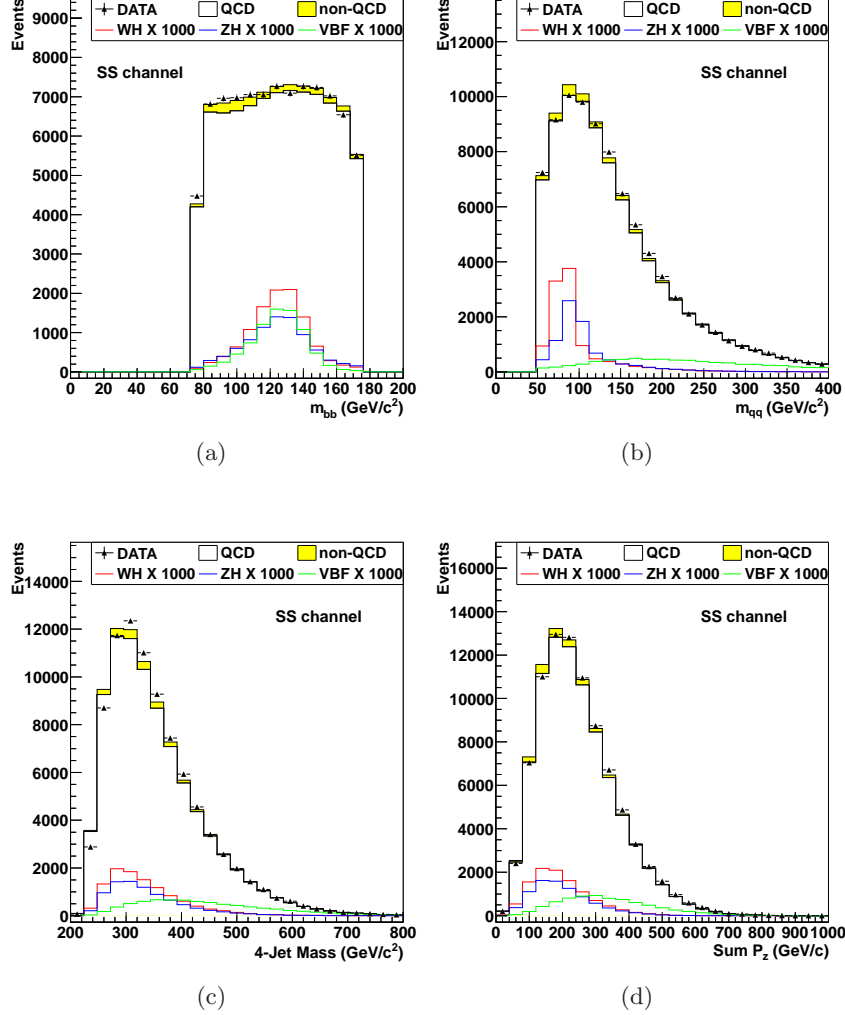


Figure 3. The QCD multi-jet background prediction (SS b -tag category) for (a) m_{bb} , (b) m_{qq} , (c) the invariant mass of four-jets system, and (d) the sum of the momenta along z direction for each of the four jets in the search signal region. The m_{qq} variable distribution is obtained after the application of the m_{qq} correction described in section 6. The black histograms are the TRF derived predictions for the QCD multi-jet background, and the black triangles are the data. The yellow histogram shows the MC predicted non-QCD background which is the sum of $t\bar{t}$, single-top, Z +jets, $W + HF$, and diboson contributions. The predicted distributions for WH events (red), ZH events (blue), and VBF events (green) for a Higgs mass of $m_H = 125 \text{ GeV}/c^2$ scaled by a factor of 1000 are also shown.

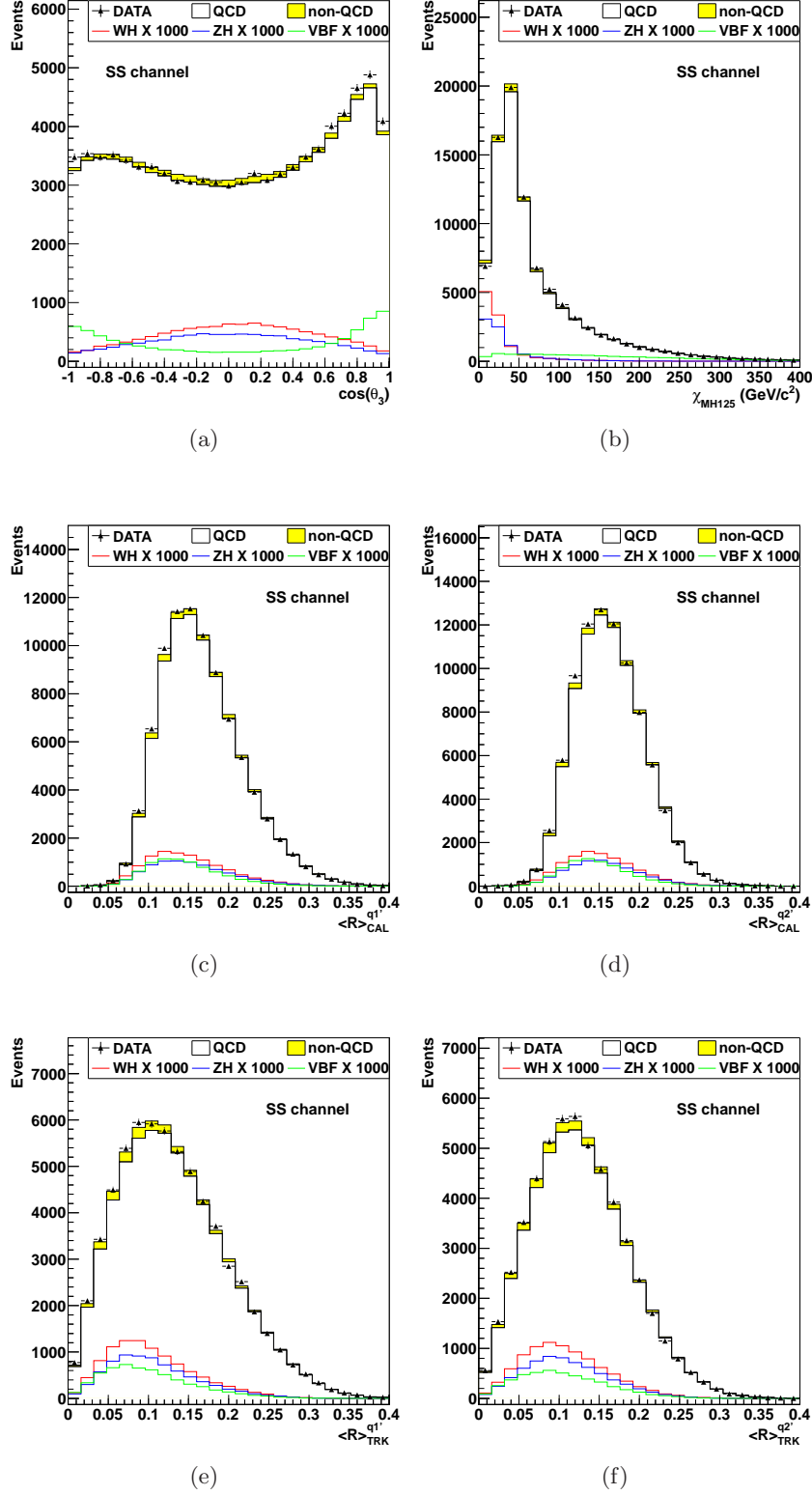


Figure 4. The QCD multi-jet background predictions for the SS b -tag category of (a) the cosine of the leading-jet scattering angle in the four-jet rest-frame [27], (b) the χ variable [11], (c) the calorimeter jet width of the first and (d) second leading untagged jet, and (e) the tracker jet width of the first and (f) second leading untagged jet. Descriptions of the signal and background histograms can be found in the caption of figure 3.

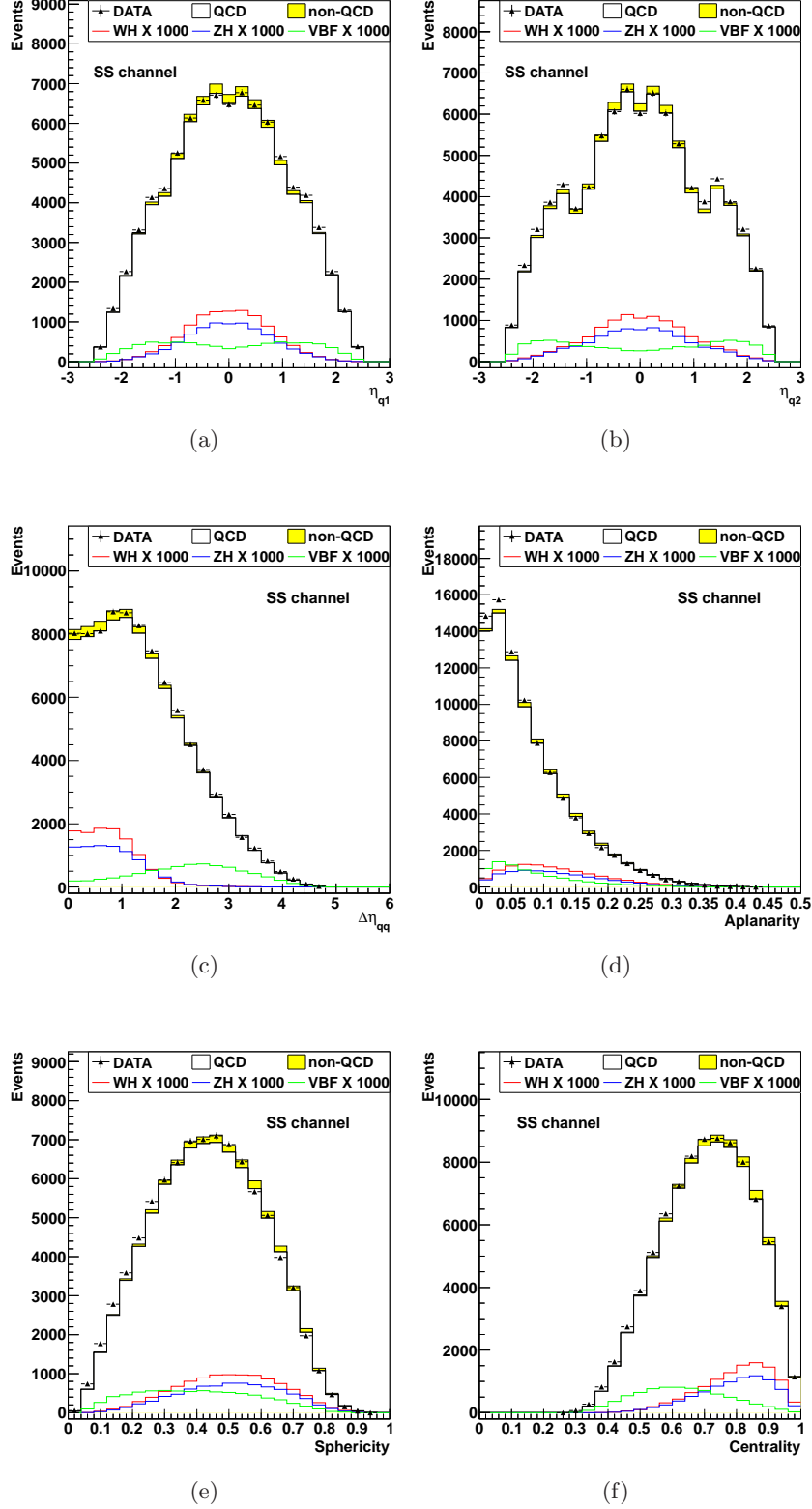


Figure 5. The QCD multi-jet background prediction for the SS b -tag category of (a) the η angle of the first leading untagged jet and (b) second leading untagged jet, (c) $\Delta\eta$ of the two untagged jets, (d) the aplanarity [20], (e) the sphericity [20], and (f) centrality [20]. Descriptions of the signal and background histograms can be found in the caption of figure 3.

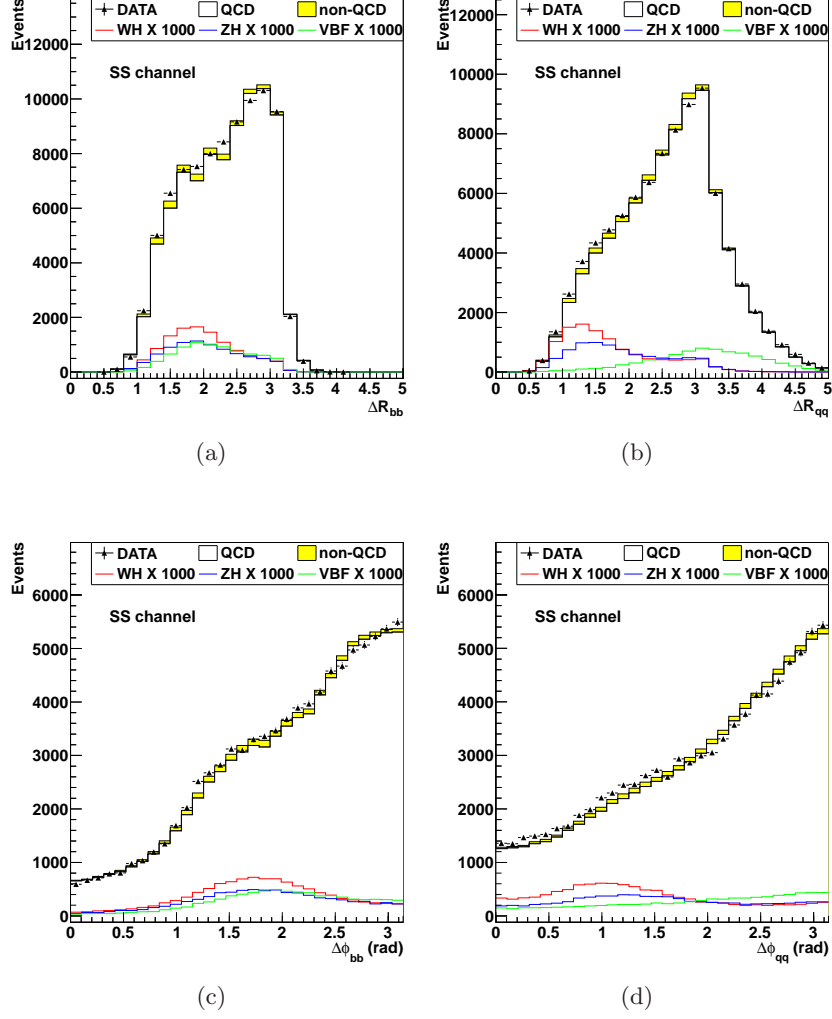


Figure 6. The QCD multi-jet background prediction for the SS b -tag category of (a) the ΔR of the two b -tagged jets and (b) of the two untagged jets, (c) the $\Delta\phi$ of the two b -tagged jets and (d) of the two untagged jets. Descriptions of the signal and background histograms can be found in the caption of figure 3.

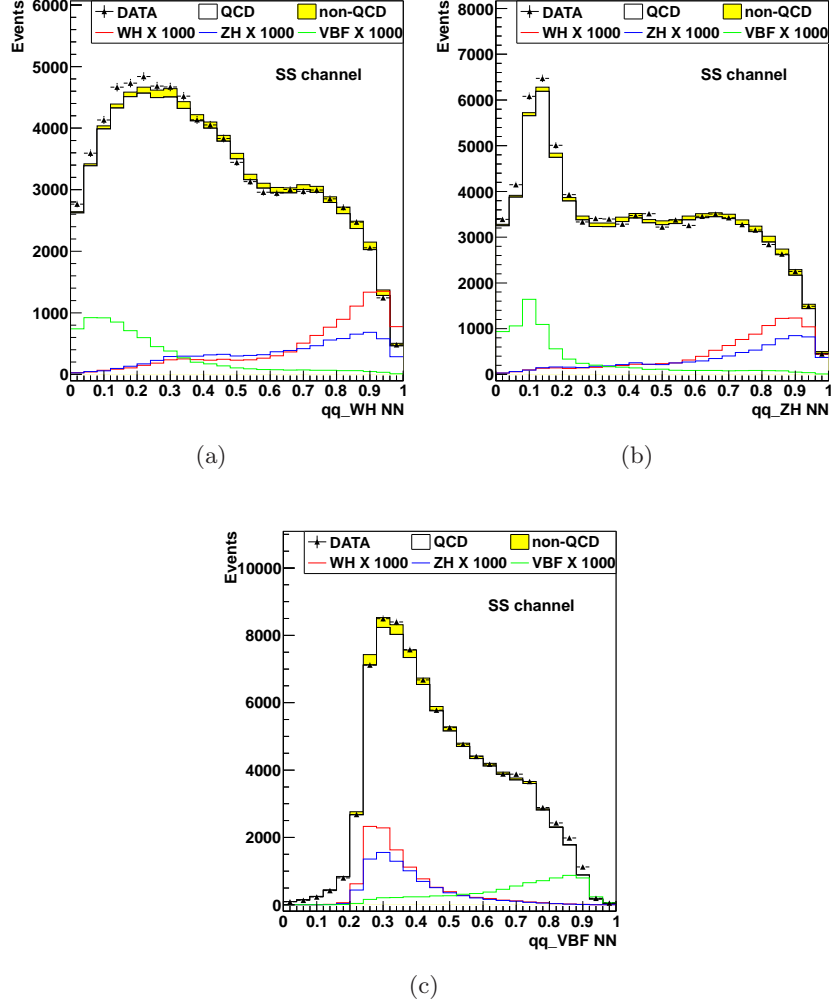


Figure 7. The QCD multi-jet background prediction for the SS b -tag category of the (a) qq_WH NN, (b) qq_ZH NN, and (c) qq_VBF NN (section 8). Descriptions of the signal and background histograms can be found in the caption of figure 3.

The WH -NN, ZH -NN, and VBF-NN are trained using dedicated MC samples for signal modeling. A small subset (10%) of single-tagged jet events, after random selection and application of the TRF, is used as the QCD multi-jet training sample. The remaining 90% of events are reserved for modeling the NN output distributions. As the shapes of the kinematic distributions are found to be consistent for both b -tagging categories, the NN is trained using SS events.

The search focuses on Higgs boson mass hypotheses in the range $100 \leq m_H \leq 150 \text{ GeV}/c^2$ at $5 \text{ GeV}/c^2$ intervals. The sensitivity of the search is improved by using separate trainings at three specific Higgs boson masses: $100 \text{ GeV}/c^2$, $120 \text{ GeV}/c^2$, and $140 \text{ GeV}/c^2$. For each Higgs boson mass hypothesis, we choose the training that gives the best search sensitivity.

Only variables that are well modeled by the TRF are used to train the WH -NN, ZH -NN, and VBF-NN. As a further validation, the modeled outputs of the WH , ZH , and VBF networks are compared to TAG events in data. The WH , ZH networks are found to be well modeled, but the VBF-NN requires an additional correction, analogous to the re-weighting performed to correct m_{qq} (section 6). Figure 8 shows the Higgs-NN distribution of $125 \text{ GeV}/c^2$ Higgs boson events with both b jets tagged by SecVtx, after the VBF-NN correction function was applied. The histogram shows the data, a stacked distribution of the backgrounds, and the Higgs boson signal scaled by 1000. As the QCD multi-jet background is large, it is difficult to see the non-QCD contributions and the QCD uncertainty. In the lower QCD subtracted data plot, it is easier to see how well the background is modeled. This plot shows the QCD uncertainty is as large as the total non-QCD contributions and the QCD subtracted data is consistent with the non-QCD background and the QCD uncertainty.

11 Systematic uncertainties

This search considered systematic effects that affect the normalization (rate systematic uncertainty) and the output (shape systematic uncertainty) of the Higgs-NN for the signal and background. The rate systematic uncertainties are defined as the variations of the number of events that pass the selection requirements. The shape-related systematic uncertainties are expressed as fractional changes in the binned distributions.

The systematic effects that affect the normalization of the Higgs boson and non-QCD background are the uncertainty on the jet energy scale (JES) [17], on the PDF, b -tagging scale factor, initial and final state radiation (ISR and FSR), trigger efficiency, integrated luminosity, and cross section [5]. The effects that affect the shape of the Higgs boson and non-QCD backgrounds are the uncertainties on the JES, ISR, FSR, and the jet width. The shape uncertainties are evaluated by adjusting their values by $\pm 1\sigma$, and propagating this change through the event selection and Higgs-NN. Table 2 summarizes all systematic uncertainties.

Only shape uncertainties are considered for the QCD multi-jet component, the normalization is unconstrained. The TRF QCD shape uncertainties arise from uncertainties in the interpolation, m_{qq} and VBF-NN correction functions. The TRF shape uncertainty

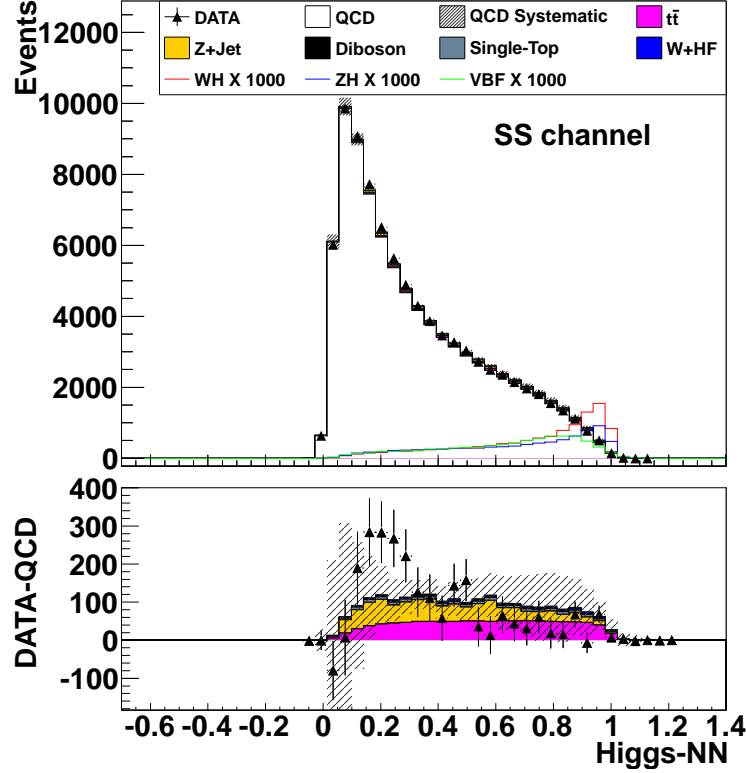


Figure 8. Higgs-NN distribution of $125 \text{ GeV}/c^2$ Higgs boson events with both b jets tagged by SecVtx, after the VBF-NN correction function was applied. All backgrounds are stacked and the superimposed Higgs boson signal is scaled by 1000. As the QCD multi-jet background is large, plots of the difference of data and QCD multi-jet are plotted with a stacked plot of non-QCD background and QCD multi-jet systematic uncertainty. Both plots show the data are consistent with the background, especially at large Higgs-NN score where the higgs signal peaks.

is defined as the shape difference of the nominal QCD shape and a systematically shifted version.

The interpolation uncertainty accounts for sample-dependence of the TRF. A TRF is measured in the TAG region to its application in the signal region. Another TRF is measured in the CONTROL region (figure 1) and is applied to the signal region. The shape difference of the nominal TAG TRF and the CONTROL TRF defines the interpolation uncertainty.

The m_{qq} and VBF-NN distributions require an additional correction to improve their TRF modeling (sections 6 and 10). The nominal correction functions are measured in the TAG region and an alternative is measured in the CONTROL (m_{qq}) and NJET6 (VBF-NN) regions. The shape difference between the usage of the nominal and alternative correction function defines the correction function shape uncertainty.

TRF (QCD multi-jet) uncertainties	
TRF interpolation	Shape
TRF m_{qq} correction	Shape
TRF VBF-NN correction	Shape
Signal and Background uncertainties	
Luminosity	$\pm 6\%$ Rate
Trigger	$\pm 3.55\%$ Rate
SecVtx+SecVtx	$\pm 7.1\%$ Rate
SecVtx+JetProb	$\pm 6.4\%$ Rate
Jet Energy Correction	$\pm 9\%$ Rate
	Shape
Jet width	Shape
Cross section uncertainties	
$t\bar{t}$ and single-top	$\pm 7\%$ Rate
Diboson (WW/WZ/ZZ)	$\pm 6\%$ Rate
$W+HF$ and Z +jets	$\pm 50\%$ Rate
WH/ZH	$\pm 5\%$ Rate
VBF	$\pm 10\%$ Rate
Signal uncertainties	
PDF	$\pm 2\%$ Rate
ISR/FSR	$\pm 3\%$ Rate
	Shape

Table 2. Summary of all systematic uncertainties.

12 Results

The Higgs-NN output distribution in data is compared to the background predictions. No evidence of a Higgs boson signal is found, nor any disagreement between the predicted background and observed data. Upper exclusion limits are calculated on the Higgs boson cross-section at the 95% CL. The limits are calculated using a Bayesian method with a non-negative flat prior for the signal cross section. We integrate over Gaussian priors for the systematic uncertainties, truncated to ensure that no prediction is negative, and incorporate correlated rate and shape uncertainties as well as uncorrelated bin-by-bin statistical uncertainties [28]. Figure 9 and table 3 show the limits from the combination of SS and SJ b -tagging categories. The observed limits agree with the expected limits.

13 Summary

A search for the Higgs boson is performed in the all-hadronic final state using 9.45 fb^{-1} of data collected by the CDF II detector. The results discussed in this paper have halved the expected limit of the previous search [11]. Half of the improvement comes from additional

Higgs mass (GeV/c^2)	-2σ	-1σ	Median	$+1\sigma$	$+2\sigma$	Observed
100	1.4	3.6	7.7	14.5	24.4	10.9
105	1.8	3.8	7.5	13.6	22.3	7.5
110	2.0	4.0	7.6	13.2	21.7	7.0
115	2.3	4.4	8.3	14.5	23.4	7.2
120	2.4	4.6	8.9	15.6	25.3	8.4
125	2.8	5.7	11.0	19.5	31.6	9.0
130	3.4	7.1	13.8	24.3	39.5	13.2
135	5.3	10.8	19.5	32.2	49.6	21.2
140	7.3	14.3	25.8	42.7	66.1	26.2
145	10.2	20.4	36.7	60.5	93.4	35.1
150	17.1	32.5	58.7	98.2	152.0	64.6

Table 3. Expected and observed 95% CL upper limits for the combined SS and SJ channels. The limits are relative to the expected Higgs cross section.

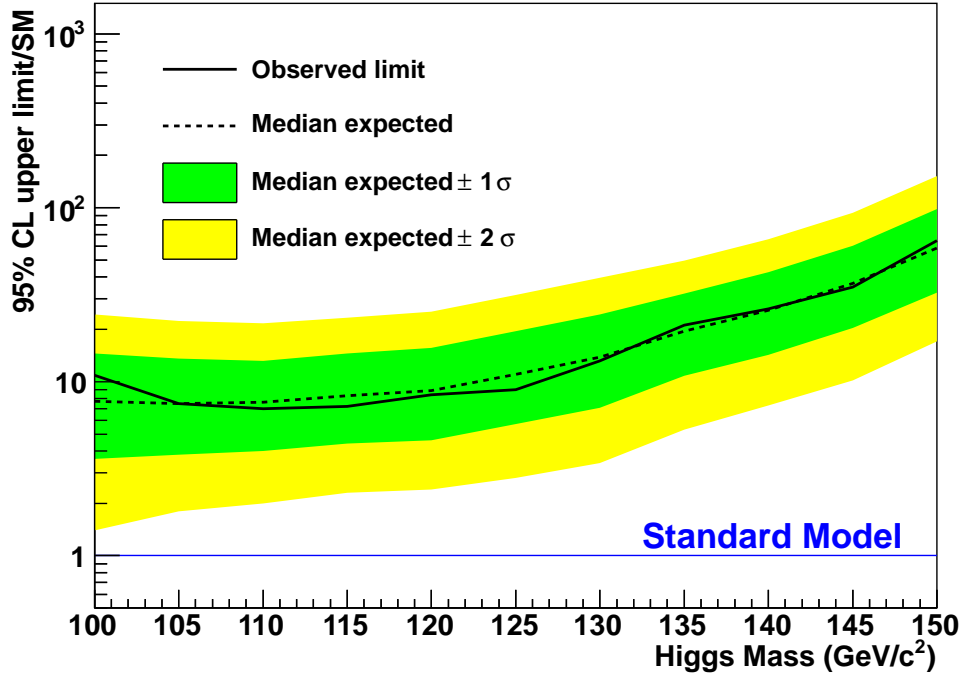


Figure 9. Upper limits at 95% CL for combined SS and SJ channels: the expected and observed limits are plotted as a function of the Higgs boson mass. The limits are relative to the expected SM Higgs boson production, which includes the $H \rightarrow b\bar{b}$ branching ratio.

data and the expanded signal region contributes an additional 17%. The reduction of the b -jet energy resolution by 18%, adding a new jet width measurement, improving the QCD multi-jet modeling, and adding more variables in the Higgs neural network and improving

its training contributes another 24%. The combination of multi-variate techniques improved the best signal-to-background ratio from 0.0007, if the m_{bb} distribution alone was used for the search, to 0.006, which is almost a ten-fold increase. No significant Higgs boson signal is observed and upper exclusion limits are set on the observed Higgs cross section relative to the SM rate as a function of Higgs boson mass in the range 100-150 GeV/ c^2 . For a 125 GeV/ c^2 Higgs boson, the 95% CL expected (observed) limit is 11.0 (9.0) times the expected SM rate. This search is CDF's fourth most sensitive $H \rightarrow b\bar{b}$ search and is more sensitive than CDF's $t\bar{t}H$ [29] and similar to CDF's $H \rightarrow \gamma\gamma$ [30] searches, which have an expected limit of 12.6 and 9.9 for a 125 GeV/ c^2 Higgs boson, respectively. CDF has also developed an improved algorithm to identify (tag) b -jets [31], which improves the b -tagging rate from 39% to 54% and was used in the latest $ZH \rightarrow \ell\ell b\bar{b}$ [32] and $WH \rightarrow \ell\nu b\bar{b}$ [33] searches. The addition of new b -jet tagger could potentially improve this search's expected limit by an additional 40% which would lower the expected limit to 7.9 times the expected SM rate for a 125 GeV/ c^2 Higgs boson. The all-hadronic search is a unique channel at the Tevatron that has not been explored at the LHC. The improvements described in this paper, such as the data-driven QCD multi-jet prediction, b -jet energy corrections, jet width, and two-stage NN can be applied to $H \rightarrow b\bar{b}$ searches and other multi-jet analyses at the LHC.

Acknowledgments

We thank the Fermilab staff and the technical staffs of the participating institutions for their vital contributions. This work was supported by the U.S. Department of Energy and National Science Foundation; the Italian Istituto Nazionale di Fisica Nucleare; the Ministry of Education, Culture, Sports, Science and Technology of Japan; the Natural Sciences and Engineering Research Council of Canada; the National Science Council of the Republic of China; the Swiss National Science Foundation; the A.P. Sloan Foundation; the Bundesministerium für Bildung und Forschung, Germany; the Korean World Class University Program, the National Research Foundation of Korea; the Science and Technology Facilities Council and the Royal Society, UK; the Russian Foundation for Basic Research; the Ministerio de Ciencia e Innovación, and Programa Consolider-Ingenio 2010, Spain; the Slovak R&D Agency; the Academy of Finland; and the Australian Research Council (ARC).

References

- [1] P. W. Higgs, *Broken symmetries, massless particles and gauge fields*, *Phys. Lett.* **12** (1964) 132.
- [2] F. Englert and R. Brout, *Broken Symmetry and the Mass of Gauge Vector Mesons*, *Phys. Rev. Lett.* **13** (Aug, 1964) 321.
- [3] P. W. Higgs, *Broken symmetries and the masses of gauge bosons*, *Phys. Rev. Lett.* **13** (Oct, 1964) 508.

- [4] **LEP Working Group for Higgs boson searches, ALEPH, DELPHI, L3 and OPAL Collaboration**, *Search for the standard model Higgs boson at LEP*, *Phys. Lett. B* **565** (2003) 61, [[hep-ex/0306033](#)].
- [5] **Tevatron New Physics Higgs Working Group, CDF , D0 Collaboration**, *Updated Combination of CDF and D0 Searches for Standard Model Higgs Boson Production with up to 10.0 fb⁻¹ of Data*, [arXiv:1207.0449](#).
- [6] **CMS Collaboration**, S. Chatrchyan et al., *Observation of a new boson at a mass of 125 GeV with the CMS experiment at the LHC*, [arXiv:1207.7235](#).
- [7] **ATLAS Collaboration**, G. Aad et al., *Observation of a new particle in the search for the Standard Model Higgs boson with the ATLAS detector at the LHC*, *Phys. Lett. B* **716** (2012) 1, [[arXiv:1207.7214](#)].
- [8] **CDF, D0 Collaboration**, T. Aaltonen et al., *Evidence for a particle produced in association with weak bosons and decaying to a bottom-antibottom quark pair in Higgs boson searches at the Tevatron*, *Phys. Rev. Lett.* **109** (2012) 071804, [[arXiv:1207.6436](#)].
- [9] A. Djouadi, J. Kalinowski, and M. Spira, *HDECAY: A program for Higgs boson decays in the standard model and its supersymmetric extension*, *Comput. Phys. Commun.* **108** (1998) 56, [[hep-ph/9704448v1](#)].
- [10] **CDF Collaboration**, T. Aaltonen et al., *Search for the Associated Production of the Standard-Model Higgs Boson in the All-Hadronic Channel*, *Phys. Rev. Lett.* **103** (2009) 221801, [[arXiv:0907.0810](#)].
- [11] **CDF Collaboration**, T. Aaltonen et al., *Search for the Higgs boson in the all-hadronic final state using the CDF II detector*, *Phys. Rev. D* **84** (2011) 52010, [[arXiv:1102.0024](#)].
- [12] **CDF Collaboration**, F. Abe et al., *Search for Higgs Bosons Produced in Association with a Vector Boson in p anti- p Collisions at $\sqrt{s}=1.8$ TeV*, *Phys. Rev. Lett.* **81** (1998) 5748.
- [13] **CDF Collaboration**, D. E. Acosta et al., *Measurement of the J/ψ meson and b -hadron production cross sections in $p\bar{p}$ collisions at $\sqrt{s} = 1960$ GeV*, *Phys. Rev. D* **71** (2005) 032001, [[hep-ex/0412071](#)].
- [14] **CDF Collaboration**, D. E. Acosta et al., *Measurement of the $t\bar{t}$ production cross section in $p\bar{p}$ collisions at $\sqrt{s} = 1.96$ TeV using lepton + jets events with secondary vertex b -tagging*, *Phys. Rev. D* **71** (2005) 052003, [[hep-ex/0410041](#)].
- [15] **CDF Collaboration**, A. Abulencia et al., *Measurements of Inclusive W and Z Cross Sections in $p\bar{p}$ Collisions at $\sqrt{s} = 1.96$ TeV*, *J. Phys. G* **34** (2007) 2457, [[hep-ex/0508029](#)].
- [16] **CDF Collaboration**, F. Abe et al., *The Topology of three jet events in $p\bar{p}$ collisions at $\sqrt{s} = 1.8$ TeV*, *Phys. Rev. D* **45** (1992) 1448.
- [17] **CDF Collaboration**, A. Bhatti et al., *Determination of the jet energy scale at the Collider Detector at Fermilab*, *Nucl. Instrum. Methods A* **566** (2006) 375, [[hep-ex/0510047](#)].
- [18] **CDF Collaboration**, A. Abulencia et al., *Measurement of the $t\bar{t}$ Production Cross Section in $p\bar{p}$ collisions at $\sqrt{s} = 1.96$ -TeV using Lepton + Jets Events with Jet Probability b -tagging*, *Phys. Rev. D* **74** (2006) 072006, [[hep-ex/0607035](#)].
- [19] M. L. Mangano, M. Moretti, F. Piccinini, R. Pittau, and A. D. Polosa, *ALPGEN, a generator for hard multiparton processes in hadronic collisions*, *JHEP* **07** (2003) 1, [[hep-ph/0206293](#)].
- [20] T. Sjöstrand et al., *PYTHIA 6.2: Physics and manual*, [hep-ph/0108264](#).

- [21] H. Lai et al., *Global QCD Analysis of Parton Structure of the Nucleon: CTEQ5 Parton Distributions*, *Eur. Phys. J. C.* **12** (2000) 375, [[hep-ph/9903282](#)].
- [22] E. Gerchtein and M. Paulini, *CDF detector simulation framework and performance*, [physics/0306031](#).
- [23] R. Brun et al., *GEANT 3: user's guide for Geant 3.10, Geant 3.11*, CERN-DD-EE-84-01 (1987).
- [24] A. Hoecker et al., *TMVA: Toolkit for multivariate data analysis*, [physics/0703039](#).
- [25] R. Brun and F. Rademakers, *ROOT - An Object Oriented Data Analysis Framework*, *Nucl. Inst. and Math. in Phys. Res. A* **389** (1997) 81.
- [26] T. Aaltonen, A. Bazatu, B. Kilminster, Y. Nagai, and W. Yao, *Improved b -jet Energy Correction for $H \rightarrow b\bar{b}$ Searches at CDF*, [arXiv:1107.3026](#).
- [27] S. Geer and T. Asakawa, *Analysis of multijet events produced at high energy hadron colliders*, *Phys. Rev. D* **53** (1996) 4793, [[hep-ph/9510351](#)].
- [28] **CDF** Collaboration, T. Aaltonen et al., *Combination of Tevatron Searches for the Standard Model Higgs Boson in the W^+W^- Decay Mode*, *Phys. Rev. Lett.* **104** (2010) 061802, [[arXiv:1001.4162](#)].
- [29] **CDF** Collaboration, T. Aaltonen et al., *Search for the standard model Higgs boson produced in association with top quarks using the full CDF data set*, [arXiv:1208.2662](#).
- [30] **CDF** Collaboration, T. Aaltonen et al., *Search for a Higgs boson in the diphoton final state using the full CDF data set from $p\bar{p}$ collisions at $\sqrt{s}=1.96$ TeV*, *Phys. Lett. B* **717** (2012) 173, [[arXiv:1207.6386](#)].
- [31] J. Freeman, T. Junk, M. Kirby, Y. Oksuzian, T. Phillips, F. Snider, M. Trovato, J. Vizan, and W. Yao, *Introduction to HOBIT, a b -jet identification tagger at the CDF experiment optimized for light Higgs boson searches*, *NIM* **697** (2013) 64, [[arXiv:1205.1812](#)].
- [32] **CDF** Collaboration, T. Aaltonen et al., *Search for the Standard Model Higgs Boson Decaying to a $b\bar{b}$ Pair in Events with Two Oppositely Charged Leptons Using the Full CDF Data Set*, *Phys. Rev. Lett.* **109** (2012) 111803, [[arXiv:1207.1704](#)].
- [33] **CDF** Collaboration, T. Aaltonen et al., *Search for the Standard Model Higgs Boson Decaying to a $b\bar{b}$ Pair in Events with One Charged Lepton and Large Missing Transverse Energy Using the Full CDF Data Set*, *Phys. Rev. Lett.* **109** (2012) 111804, [[arXiv:1207.1703](#)].